# Performance and results of the Reflection Grating Spectrometers on-board XMM-Newton

J.W. den Herder[a], A.C. Brinkman[a], S.M. Kahn[b], G. Branduardi-Raymont[c], M. Audard[d], E. Behar[b], A. Blustin[c], A.J. den Boggende[a], J. Cottam[b], C. Erd[e], C. Gabriel[f], M. Güdel[d], K. van der Heyden[a], J.S. Kaastra[a], A. Kinkhabwala[b], M.A. Leutenegger[b], R. Mewe[a], F.B.S. Paerels[b], A.J.J. Raassen[a], J.R. Peterson[b], A. Pollock[f], A.P. Rasmussen[b], M. Sako[b], M. Santos-Lleo[f], K.C. Steenbrugge[a], T. Tamura[a], and C.P. de Vries[a]

[a]SRON, National Institute for Space Research, Sorbonnelaan 2, 3584 Utrecht, The Netherlands
[b]Columbia Astrophysics Laboratory, NY, 10027, USA
[c]Mullard Space Science laboratory, UCL, Holmbury St. Mary, RH5 6NT UK
[d]Paul Sherrer Institute, 5232 Villigen, Switzerland
[e]Space Science Department, ESA, 2200 AG Noordwijk, the Netherlands
[f]XMM Science Opterations Center- VILSPA, ESA, E-28080 Madrid, Spain

## ABSTRACT

XMM-Newton was launched in December 1999 and science operations started in March 2000. Following two years of very successful operations, a report on the instrument performance and a selection of exciting new results are presented.

Behind two of the three telescopes of XMM-Newton Reflection Grating Spectrometers (RGS) are placed. Each spectrometer consists of an array of reflection gratings and a set of back illuminated CCDs. They cover the wavelength band between 6 and 38 Å with a resolution varying between 100 and 600 (E/ΔE) and a maximum effective area of 140 cm$^2$ for the two spectrometers combined. The selected wavelength band covers the K-shell transitions of C, N, O, Ne, Mg and Si as well as the L- and M-shell transitions of Fe. After a short introduction to the instrument design, the in-orbit performance is given. This includes the line spread function, the wavelength scale and the effective area including their stability during the more than 2 years of operations. Following this a number of key scientific results are briefly addressed, illustrating the power of the RGS instrument in combination with the other instruments on-board of XMM-Newton as well as the wealth of information which is obtained as the RGS instruments operate continuously.

**Keywords:** X-ray instrumentation, reflection gratings, XMM-Newton

## 1. INTRODUCTION

The scientific return of XMM-Newton is greatly enhanced because the three instruments, EPIC, RGS and OM are co-aligned and always observe simultaneously. Per observation the payload offers broadband 0.2 to ∼ 14 keV spectroscopy with a modest resolving power (E/ΔE between 5 and 60); high resolution spectroscopy between 5 and 38 Å (2.5 to 0.35 keV) with a resolving power of about 400 at 0.5 keV and optical monitoring between 1700 and 6000 Å for sources with a visible magnitude between 7.4 and 23.5 (the Optical Monitor will be damaged when too bright sources are observed).

Since the spectral resolution degrades linearly with the angular resolution of the focusing optics, the moderate spatial resolution of the XMM-Newton telescopes requires a very high dispersion. For transmission gratings, which have been incorporated in Einstein, Exosat and Chandra, this requires very high line densities. These cannot be fabricated with existing technology. Reflection gratings in contrast, offer the possibility of very high dispersion with modest line densities (1000 lines/mm). With proper optimization of the grating parameters, they can also yield reasonable diffraction efficiencies in the desired spectral band and order. One advantage of this design is that the resolution degrades only slowly for moderately extended sources (broadening of the line profile is about 0.1 Å per arcmin).

## 2. INSTRUMENT DESCRIPTION

### 2.1. Instrument Design

The RGS design incorporates an array of reflection gratings placed in the converging beam at the exit from the X-ray telescope. The grating array deflects roughly half of the X-ray light to a strip of CCD detectors offset from the telescope focal plane. The remaining light passes undeflected through the grating stack where it is imaged with modest energy resolution by the EPIC instrument. The nine large back illuminated CCDs of the Reflection Grating Spectrometer are operated in frame transfer mode at a temperature of $-80^{o}$C. The read-out times are selected so that single photons are detected. The layout of the different elements is shown in Fig. 1.

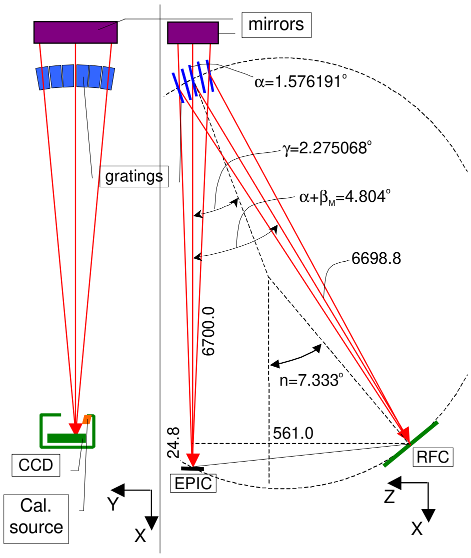


**Figure 1.** Optical lay-out of one RGS

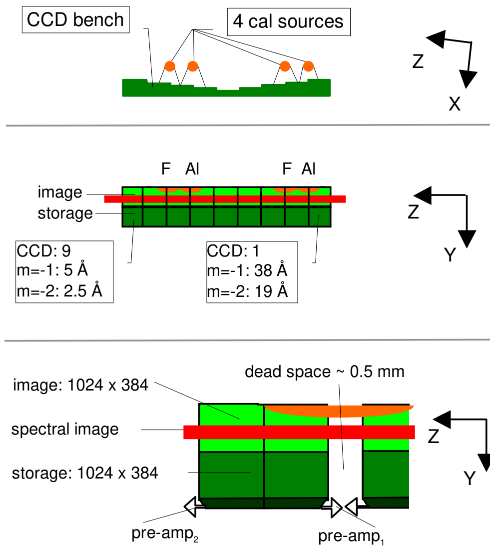


**Figure 2.** CCD detector lay-out

The reflection grating array contains 182 gratings. The gratings are mounted at grazing incidence to the beam in the in-plane classical configuration in which the incident and diffracted rays lie in a plane which is perpendicular to the grating grooves. Because the beam is converging, the gratings are not parallel but the incident angle at the center of the grating, $\alpha$, is the same for all gratings. In addition the gratings are mounted so that their centers lie on a Rowland circle, which also contains the telescope focus and the spectral detector. In this configuration aberrations, which would otherwise be due to the geometry, are eliminated. The groove density on the gratings is not constant across the grating surface to compensate for the varying incident angle over a grating. The dispersion equation of the spectrometer is given by $m\lambda = d(\cos\alpha - \cos\beta)$ where $m$ is the inside spectral order ($m < 0$), $d$ is the groove spacing, $\beta$ the angle between the outgoing ray and the grating plane and $\alpha$ is the angle between the incoming ray and the grating plane. The diffraction efficiency (in the order of 10 %) is optimized for 15 Å.

At the spectral focus the photons are detected by an array of 9 back illuminated CCDs. Back illuminated CCDs are required to enhance the low energy QE (> 80 % over the full range). To reduce the sensitivity of the devices for optical stray light, a thin (45 to 75 nm) Al layer is deposited on top of each CCD. The CCDs, which have 2 × 384 by 1024 pixels of 27 × 27 $\mu$m each, are operated in frame transfer mode. X-rays are absorbed in the CCD and generate a charge which is proportional to the X-ray energy. The image is accumulated in one half of the CCD (image section) and then quickly transferred to the other half (storage section) prior to read-out. The CCD is read-out by two low noise on-chip amplifiers which speeds up the read-out time and increases the redundancy. On-chip binning is possible and is applied. With $3 \times 3$ on-chip binning the line spread function of the instrument (typically 200 $\mu$m) is still adequately sampled. The lay-out of the detector is shown in Fig. 2 where it is also indicated that spectral orders of the gratings overlap. These can be separated by using the energy resolution of the CCDs. To monitor the performance of the CCDs, each camera is equipped with 4 on-board calibration sources which emit either Al-K (1.487 keV) or F-K (0.677 keV). The cameras are operated at $-80^{o}$C but temperatures as low as $-120^{o}$C are feasible to reduce the effect of radiation damage. In flight two CCD chains failed covering the region between 10.3 and 13.6 Å for RGS1 (CCD7) and between 19.9 and 24.9 Å for RGS2 (CCD4) which includes the important Oxygen triplet.

### 2.2. Instrument modes

Three operating modes are available with the RGS: Spectroscopy, High Time Resolution and Diagnostic mode. In the most commonly used Spectroscopy mode, the CCDs are read-out sequentially. With a typical readout time of 0.6 s per CCD the minimum accumulation time in Spectroscopy is 4.8 s. The read-out of the instrument is controlled by the on-board software. Since the timing of the instrument controller is not fully predictable, small variations (0.01 s) in the accumulation time per CCD are observed. The knowledge about integration time is, however, very good ($\pm 2\mu$s). For each photon the position and energy is measured where the position gives the X-ray energy as diffracted by the gratings. The CCD pulse height is used to separate the spectral orders. Source and background events are extracted by making appropriate selections in the cross dispersion direction and their CCD pulse height. Events are characterized on-board and events with either too low (electronic noise) or a too high charge (particles) are rejected. Also events in excess of $2 \times 2$ bins are rejected as the typical size of a true X-ray event is less than 2 bins. In Diagnostic mode the full CCD image is transferred to the ground. These data, which in normal operations are collected once every 25 minutes, allow for a detailed study of the dark current and electronic noise and hot pixel verification.

The High Time Resolution mode (HTR) allows for the shortest accumulation time of 15.32 ms per CCD. This fast read-out is achieved by summing 74 lines in the read-out register of the CCD prior to the read-out. As a consequence it is not possible to have a spatial separation of the background, increasing the background typically by a factor of 5 compared to normal Spectroscopy. Some further improvements are currently investigated which may reduce the read-out time per CCD by 40 %. The HTR mode faces similar variations in the integration time as the Spectroscopy (also giving the same accuracy about the integration time).

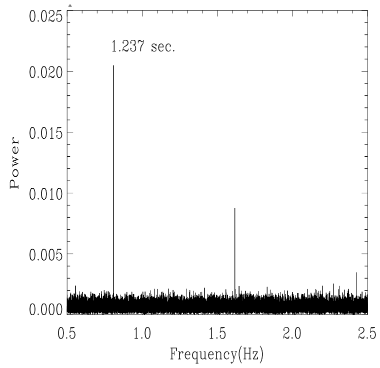


**Figure 3.** Power spectrum for the main-on state of Her X-1

Recently the HTR mode was commissioned and was used on the intermediate mass X-ray binary Her X-1. The system contains an X-ray pulsar with a 1.24 s period in the center which can be directly observed during part of time (otherwise it is obscured by a precessing tilted and wrapped accretion disk). During the time the pulsar can be directly observed (main-on state) the RGS instruments were in HTR mode. In Fig. 3 we show the power spectrum for the data in the main-on state clearly indicating the prime frequency of the neutron star, which is in good agreement with the known period of the pulsar. Also the second and third harmonics are visible. Some further measurements in the low-state, when emission lines originating from the disk or companion are visible, are planned. It is expected that the HTR mode will be made publicely available in the 3rd XMM-Newton call for proposals.

## 3. IN ORBIT PERFORMANCE

A full description of the RGS calibration aspects is given by Rasmussen et al.(15) in these proceedings. In this section we summarize some of the key results only.

### 3.1. Line Spread Function and wavelength scale

The line spread function is a convolution of the spatial mirror response, projected on the dispersion axis and the grating response. The grating response includes a small angle Gaussian scattering component and a Lorentzian wide angle scattering component. The resulting profile is also convolved with the CCD energy response which includes a tail to lower energies due to events which loose part of their charge near the surface of the CCD. The data selections to optimize the signal-to-noise and to separate orders, will make the final response clearly asymmetric (see den Herder et al. (5) for details). The shape of the line spread function is merely determined by the mechanical stability of the optical components after launch and no changes have been observed ($E/\Delta E$ between 100 and 600 in the first order varying as function of wavelength between 6 and 38 Å).

The wavelength scale is determined by the relative alignment of the various instrument units and their structural stability. During the integration on the ground the alignment could only be determined with a limited accuracy. Using a set of strong emission lines from the coronal sources Capella, HR1099 and AB Dor, the alignment parameters could be optimized in orbit. The accuracy of the wavelength for a nominal pointing on-axis is $\sim$8 mÅ (1 $\sigma$). This uncertainty can be reduced when strong lines, intrinsic to the source, are used (self-calibrating). Furthermore, it is expected that using the detected source position in the EPIC instruments, some improvement is feasible.

### 3.2. Effective area

The effective area has been verified in orbit using a number of bright sources including the BL Lac objects Mrk 421, PKS 2155-304 and the quasar 3C273. The early measurements on Mrk 421 and 3C273 have been used to optimize the physical model of the instrument (especially the scattering parameters for the gratings and the partial event description for the CCDs, details are given in 5). By repeated measurements, as is shown in Fig. 4 (38 ksec in orbit 087) and in Fig. 5 (90 ksec in orbit 362) for PKS 2155-304 it is verified that the instrument response is stable over time. Only a change in power law index and normalization is required ($\Gamma = 2.36(\pm 1)$ and $2.33(\pm 1)$ for the two observations respectively and normalization of $372(\pm 1)$ and $662(\pm 1)$ photons/m$^2$/keV at 1 keV). With this simple model the residuals are less than 10% and similar for the two observations. These residuals might be due to slightly different incidence angles on the mirrors and/or gratings in our model compared to the real hardware.

In addition the combination of many observations of simple line-free spectra of sources with low and high interstellar extinction allowed us to disentangle the interstellar component from the instrumental oxygen K-edge (see de Vries et al., 6). In Fig. 6 the ratio between a source with high extinction (6 ks observation of Sco X-1) and a combination of sources with low extinction (172 ks of Mrk421 and 346 ks of PKS 2155-304) is shown. In this ratio the instrumental O-edge features are folded out and the expected ratio, based on the best available knowledge of the cross sections near the O-edge, is shown as dashed line. Although the shape is reasonable there is a clear shift in the edge, which is not unexpected as the absolute scale for the calculated cross sections is somewhat uncertain. This is illustrated by the solid line where the edge is shifted by $0.13(\pm 1)$ Å. At 23.5 Å the 1s-2p absorption in the ISM is visible. With the improved model for the interstellar absorption, the instrumental component can now be extracted. This is shown in Fig. 7 where the solid curve gives the results for the O-edge and the range below 22 Å and above 24 Å is extrapolated using the Henke tables (9). The amount of Oxygen on the detector is rather large. This is probably due to water contained in the porous $MgF_2$ layer which insulates the active Si of the CCD from the Al light shield on top of it.

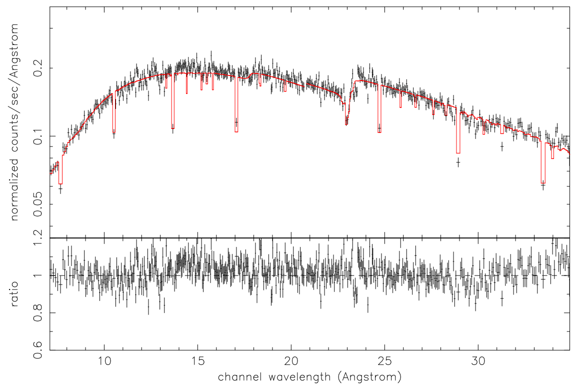


**Figure 4.** RGS1 spectrum for PKS 2155, orbit 087

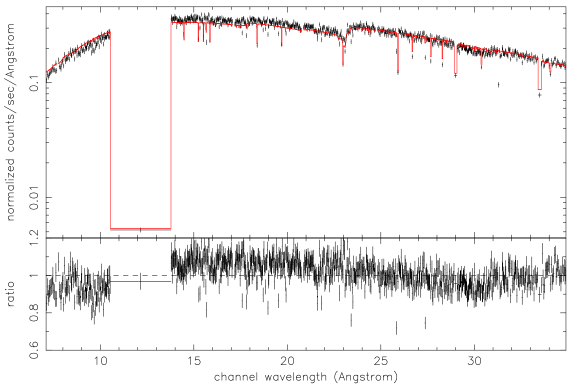


**Figure 5.** RGS1 spectrum for PKS 2155, orbit 362

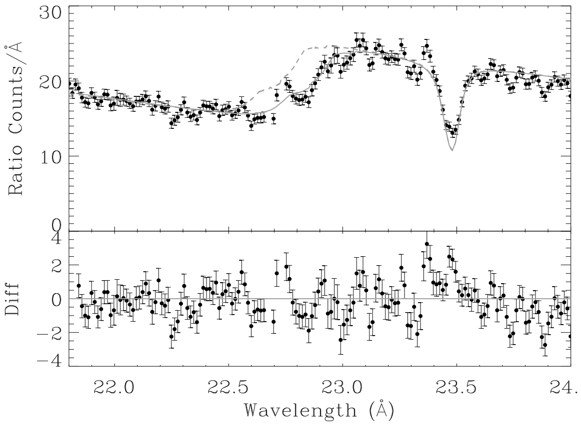


**Figure 6.** Ratio of spectra of high extinction over sources with low extinction (see text).

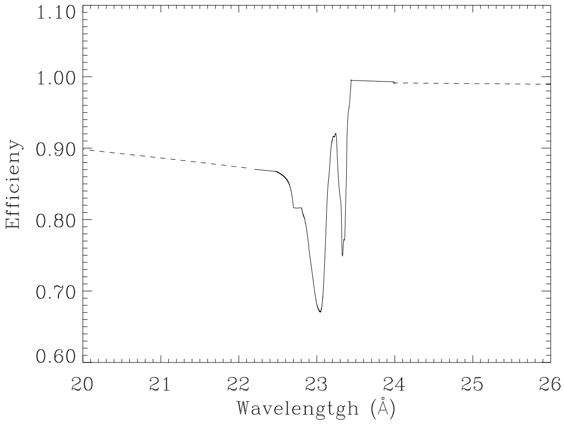


**Figure 7.** Derived instrumental efficiency around the O-edge.

### 3.3. In orbit stability

The instrument performance and its degradation over time is monitored by regular in-flight calibrations and includes verification of the line spread function and wavelength scale by observations of the coronal sources HR1099, Capella and ABDor. The effective area is monitored by the measurement of a number of sources with limited spectral features including Mrk 421, PKS 2155-304 and 3C273. Occasionally these measurements are performed simultaneously with Chandra X-ray observatory. In addition the detector performance is monitored using the events from the 4 on-board calibration sources. Comparing the relative ratio of the events for the two different types of sources (F and Al) gives information about the most likely contaminants on the detector (ice and hydro-carbons). No additional contamination is observed as the reduction of the F-K and Al-K intensity is within the error bars identical (see Fig. 8). This confirms the results from the PKS2155-304 measurements (see Fig. 4 and 5 for example) where also no change in the O-edge depth is observed. Furthermore these on-board calibration sources allow us to monitor the gain and CTI change by comparison of the known energy with the measured energy. Due to radiation damage of the CCDs (and some aging of the electronics) some change is observed (combined effect of 1 % reduction over 1 year) which is conform the pre-flight expectations. These changes can be easily calibrated. A more serious problem is the increase of the noise temperature of some pixels which, in addition, occasionally also cool down in certain periods. This is illustrated in Fig. 9 where the number of rejected pixels, defined as present in more than 5 % of the frames and not consistent with an astrophysical line, is given as a function of time. This increase is attributed to radiation damage. As result of pixel to pixel variations in the noise temperature, the selection in the CCD energy range will vary as a function of wavelength (and is also not fully stable over time). Although this effect is small (less than a few %) it may affect the interpretation of weak absorption features and/or emission lines. To reduce this effect it is planned to lower the temperature of the detectors to $-115^{o}$C.

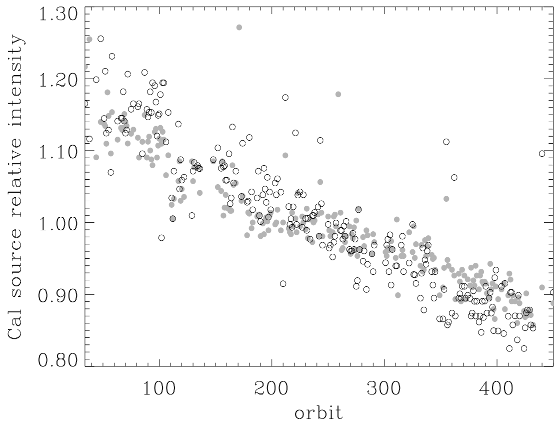


**Figure 8.** Change in intensity of the on-board calibrations sources for Al (gray dots) and F-K (open circles).

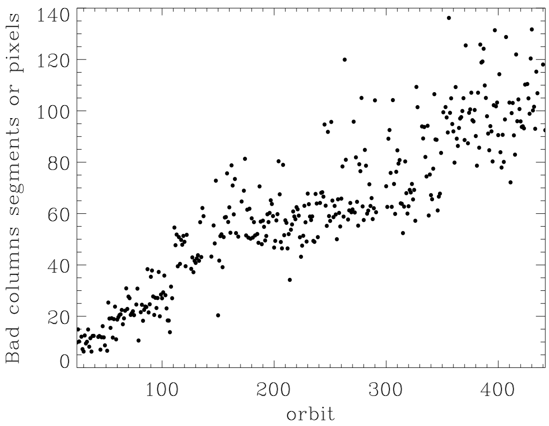


**Figure 9.** Increase in number of unusable pixels due to increased noise temperature

## 4. SCIENTIFIC HIGHLIGHTS

The large number of observations with the RGS has resulted in a number of expected and a number of unforeseen, new discoveries. Key results, as partially reported in the dedicated A&A issue (volume 365), include the observed lack of emission lines from cooled gas at 1 keV or below in clusters of galaxies (see Kaastra et al. (10), Tamura et al. (18), Peterson et al.(13) for example). Other results are the inclusion of relativistically broadenend emission lines in the modeling of spectra of some AGN (MGC -6–30-15 and Mrk 766, see Branduardi-Raymont (1) and Sako (17)) and the observation of the inverse FIP effect where the relative abundance of elements increases with the first ionisation potential (see Brinkman et al. (2) and Güdel et al. (8)). They will not be addressed in this presentation and the reader is referred to the given references.

In this section we will present a selected number of more recent results, emphasizing the diagnostic power of high resolution spectroscopy, the unique capability of the RGS instrument for moderately extended sources, the power of observations ranging from the optical into the X-ray regime and the analysis of a large set of combined measurements to set limits on the density of the local Intergalactic medium.

### 4.1. Stellar coronae and winds

Hot outer atmospheres with high densities ($n_{\rm e} > 10^{10}$ cm$^{-3}$) and very hot gas ($T > 1 - 10$ MK) are ubiquitous in stars. The corresponding X-ray spectra exhibit bright emission lines of hydrogen-like and helium-like ions of nitrogen, oxygen, neon, magnesium, and silicon as well as a number of weaker lines from other transitions. In this section we concentrate on the 20 to 30 Å region which includes the helium-like triplet of oxygen (21.60, 21.80 and 22.10 Å) and the hydrogen-like emission line of nitrogen (24.78 Å). In Fig. 10 to 12 the spectra are shown for Procyon (optically bright; late type F; at 3.5 pc), $\tau$ Sco (type OB; 130 pc) and $\zeta$ Puppis (brightest O star; 450 pc). Line features are clearly seen in all three spectra which can be studied.

From these data it is immediately clear that high resolution spectra provide a unique diagnostic tool to study details of the physical conditions in these hot outer envelopes. In the spectra of Procyon and $\tau$ Sco the He-like triplets are clearly separated. In absence of a radiation field, the ratio $G = (f + i)/r$ and $R = (f/i)$ where $r, i$ and $f$ are the resonance, inter-combination and forbidden line fluxes, are good tracers for the temperature of

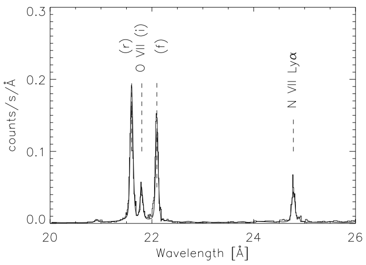


**Figure 10.** Spectrum of Procyon

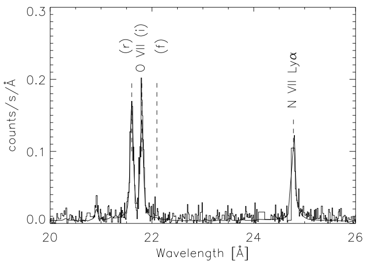


**Figure 11.** Spectrum of $\tau$ Sco

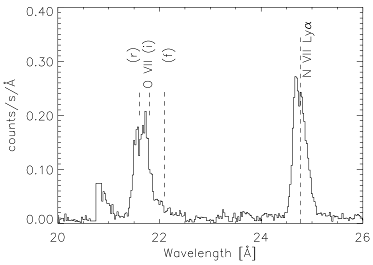


**Figure 12.** Spectrum of $\zeta$ Puppis

the plasma and the density. In the presence of a strong UV field the forbidden line level ($1s2s^3S_1$) can be de-populated by the absorption of a UV photon and the inter-combination line level ($1s2p^3P_{1,2}$) can be populated (see Porquet et al. (14)). This is indeed observed in the $\tau$ Sco spectrum where the forbidden line is almost absent due to the much more intense stellar UV field (32000 K instead of 5500 K for Procyon). In the spectrum of $\zeta$ Puppis the He-like triplets are not resolved anymore. The broad line profiles ($\sim$ 1000 km/s) are indicative of the hot plasma that is flowing outward with the stellar wind. This is confirmed by the fact that we do not see strong attenuation at low energies, which confirms that the X-ray emitting regions are not concentrated at the base of the winds (see Kahn et al., 11).

### 4.2. Stellar Flares from optical to X-rays

Stellar coronae are thought to derive their thermal energy from magnetic fields anchored in the photosphere. The mechanisms that heat the plasma to $10^6 - 10^7$ K are not well understood. During flaring episodes, magnetic reconnection is believed to explosively release energy stored in non-potential magnetic fields. A large fraction of the energy is channeled into energetic electrons ($>$ 10 keV) that travel along the magnetic fields and heat cooler plasma (chromospheric) to coronal temperatures. The resulting overpressure drives the material into the coronal magnetic loops where it cools by radiation and conduction. During a 60 ks observation of a close-by star Proxima Centauri (see Güdel et al., (7)) a huge optical and X-ray flare occurred. This is shown in Fig. 13 where in the top panel the total flux as measured in the EPIC PN camera is shown together with the optical light curve, measured by the Optical Monitor of XMM-Newton. The time derivative of the X-ray light curve (bottom left panel) closely resembles the optical light curve until after the optical peak when uncorrelated cooling mechanisms take over. This provides evidence that the initial energy release, possibly in the form of high-energy particles, drives matter into the corona (the chromospheric evaporation scenario). In the bottom right panel the first evidence for density modulations during a stellar flare is shown. The emission line triplets of O VII and Ne IX are formed by radiative decay to the ground state. In cool stars with negligible UV radiation the flux ratio $R = f/i$ is sensitive to the electron density because electron collisions can excite the $^3S_1$ to the $^3P$ state before the former decays radiatively. The characteristic electron density derived from the O VII triplet, changes about two orders of magnitude. Qualitatively similar variations are seen in the Ne IX triplet. These results are in agreement with the evaporation scenario in which the density increases when material is heated and lifted in the corona.

### 4.3. Emission and absorption line spectra of AGN

Active Galactic Nuclei are the sites of rather violent phenomena. Gas is being swallowed by the black hole, which is fed by a continuous supply of fresh material through the accretion disk. This process produces high energy radiation at the inner parts of the disks and in the immediate environment of the black hole. Depending on the viewing direction with respect to the absorbing gas expected to surround the nucleus (i.e. whether the primary radiation source is visible) AGNs can be grouped. In Seyfert 1 galaxies a significant fractio of the radiation will be absorbed by ionized gas and absorption lines are observed. In Seyfert 2 galaxies the absorption will be so great that only the reprocessed emission from the diffuse gas, exposed to the radiation from the obscured

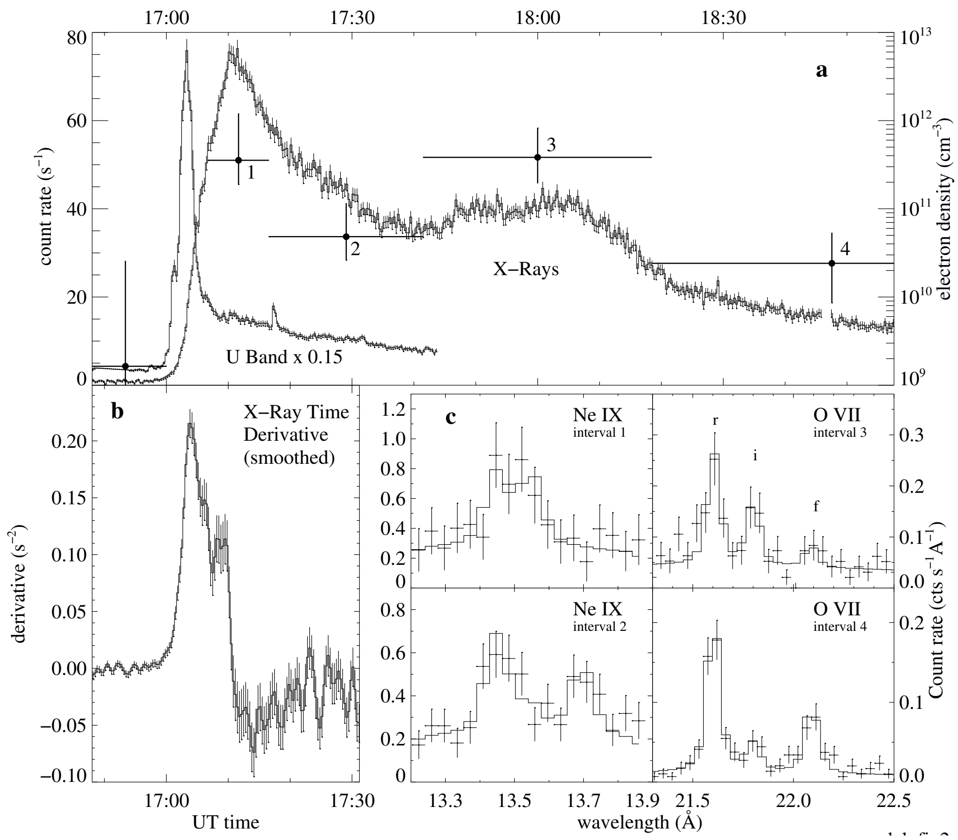


**Figure 13.** Light curves for a strong flare in the X-ray band and the UV band as well as the change in the He-like triplets due to density variations

primary source, is observed. In this case the continuum of the central nuclear component is completely absorbed by the dusty torus around the central object.

In Fig. 14 we show the spectrum of the prototype Seyfert 2 galaxy NGC 1068 (see 12 for more details). The spectrum is dominated by line emission. Apart from the n = 1 → 2 transitions and numerous Fe L-shell emission lines we also see many higher order resonance transitions (1s → np) in H-like and He-like ions. Most emission lines appear to be broadened and shifted. Blueshifts from roughly 0 to 600 km s$^{-1}$ have been measured and the line widths (between 300 and 700 km s$^{-1}$) are due to intrinsic velocity distributions in the source. The spectra include also a very distinctive radiative recombination continua (RRC) for H-like and He-like C, N and O. They are produced when electrons recombine directly to the ground state of these highly ionized species. RRC are broad features for hot, collisionally ionized plasma but are narrow for cooler photo-ionized plasma. The derived temperatures are consistent with a range of $kT_e \sim$ few eV which suggest that the plasma is photo-ionized. Further information about the physical conditions in the plasma can be deduced from detailed comparison of the spectra with model predictions. In Fig. 15 the spectrum around the O VII triplet is shown. In the bottom panel the model includes recombination and radiative cascade following photoionization. In this model the emission in all resonance lines np → 1s is underestimated. Adding photoexcitation in a self consistent way, the agreement between the data and the model improves considerably (top panel of Fig. 15).

In Fig. 16 we show the RGS spectrum of NGC 5548, a Seyfert 1 galaxy (at redshift z = 0.0168) and in Fig. 17 we show a detail of the same spectrum, including a model based on continuum radiation (power law and a modified black body) plus a highly ionized gas in the warm absorber. To describe the spectrum we need a rather high ionization parameter, $\xi = 490$. Also the importance of Fe as an absorber is amply visible in this

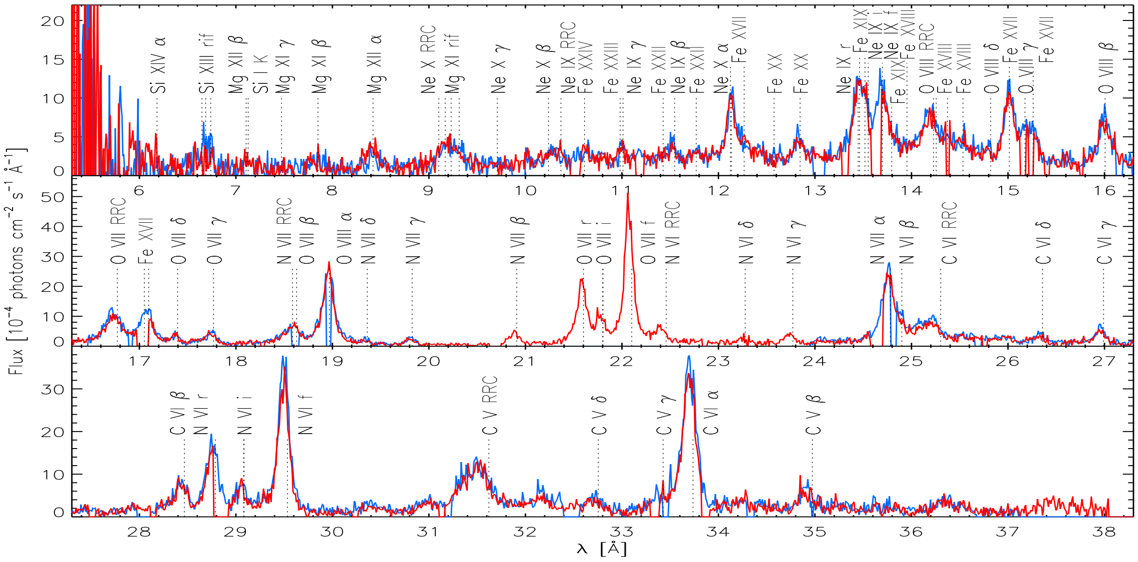


**Figure 14.** RGS spectrum of NGC 1068

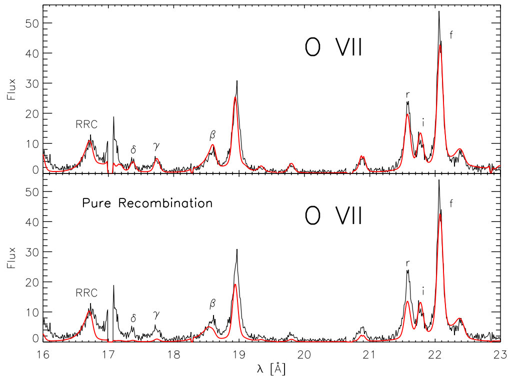


**Figure 15.** Data and model for part of the NGC 1068 spectrum for recombination/ radiative cascade following photoionization and radiative decay following photo-excitation (top) or recombination/radiative decay alone (bottom).

plot. Absorption from Ne and O is observed: for O VIII we see the Lyman $\beta$, $\gamma$ and possibly $\delta$ and $\epsilon$ lines as well. These higher order lines are important diagnostic tools as the Ly$\alpha$ and Ly$\beta$ lines are saturated. The width of the forbidden O VII line (in emission) gives directly the velocity broadening of this line and, in this case, suggests that it is formed at rather large distance from the central ionizing source.

### 4.4. High resolution spectroscopy of moderately extended sources

The spatial resolution of the Chandra mirrors is superb for extended sources. XMM-Newton offers, in addition, a large effective area combined with simultaneous broadband spectroscopy (EPIC) and the high resolution spectroscopy (RGS). This allow for an even more detailed test of various models. This is illustrated by the analysis of the SNR N103B, which is the fourth brightest X-ray remnant in the LMC (see 19). In Fig. 18 the spectrum obtained with RGS is shown. Clearly visible are the various transitions despite the degradation of the resolution due to the spatial extent of the source (0.5 arcmin). Also shown is the EPIC-MOS spectrum (Fig.19) where emission from He-like S, Ar, Ca as well as an Fe-K blend at 6.5 keV are clearly observed. The data can be

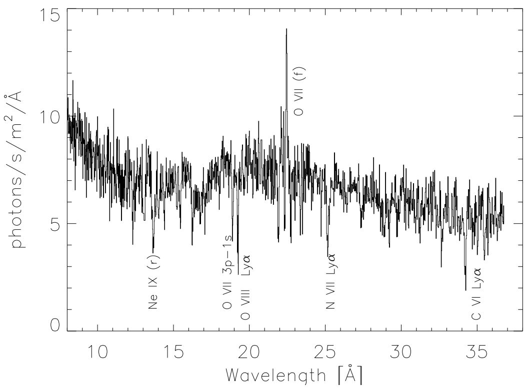


**Figure 16.** RGS spectrum of NGC 5548

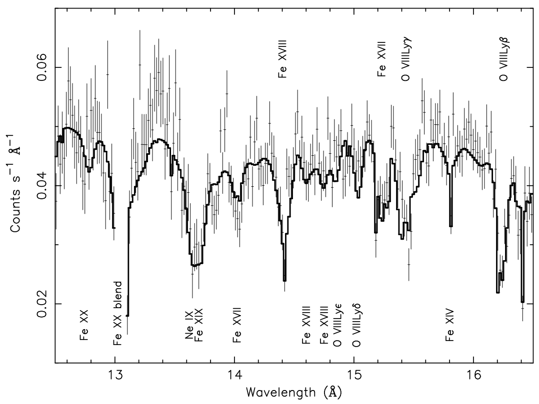


**Figure 17.** Selected part of the spectrum of NGC 5548

described by both a Collisional Ionization Equilibrium (CIE) and a non-equilibrium ionization model (NEI). For the RGS spectra two temperature components are sufficient: one component of $kT_e = 0.65$keV which produces the Fe-L component and a second, weaker and cooler, component which produces most of the oxygen emission. Although the temperature of this component is quite different for the CIE and NEI models (0.2 keV and 0.55 keV) the data cannot distinguish between them (nor are the other components sensitive to this difference). From the EPIC spectrum it is clear that the source also has a hot component (3.5 keV). The derived redshift is consistent with the radial velocity of the LMC. With the use of the Chandra data, obtained with the ACIS camera, we clearly see a difference in the morphology for the three temperature components, which suggests that they are probably unrelated dynamically. The clear presence of the O, Ne and Mg emission in the RGS spectra indicates that N103B might be the result of a type II SN and not a type Ia as previously thought.

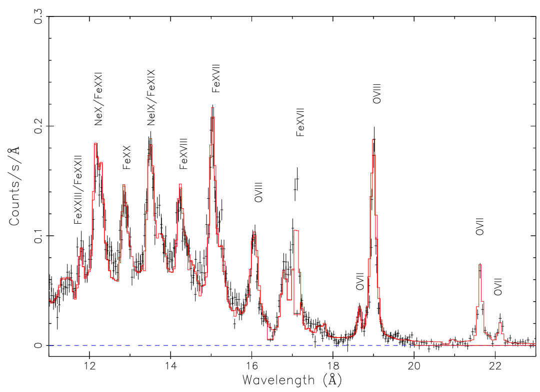


**Figure 18.** RGS spectrum of N103B. The model is the best fit 2 component NEI model plus an underlying continuum ($kT_e = 3.5$ keV).

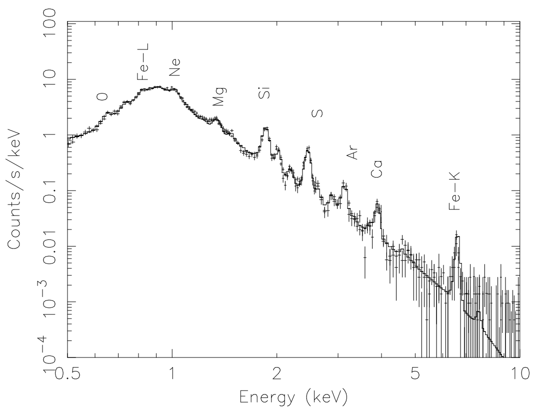


**Figure 19.** EPIC-MOS spectrum of N103B (20 ks, 7 August 2000). The most prominent line blends are labeled.

### 4.5. Detection of the nearby Intergalactic Medium

By the combination of a set of very long exposures of 3C273 (about 417 ks, $z = 0.158$), Mrk 421 (280 ks, $z = 0.031$) and PKS 2155-304 (255 ks, $z = 0.116$) it is possible to identify features which can be attributed to absorption in the nearby intergalactic medium (see 16). In Fig. 21 the spectra are shown between 18.3 and 25.3 Å. Absoprtion features due to O VII (at 18.62, 21.60 Å) can be identified as well as possibly some

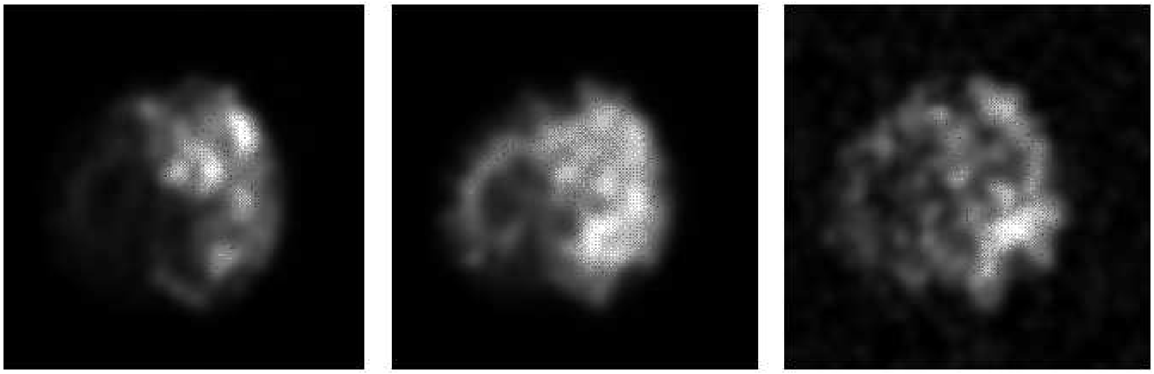

**Figure 20.** Chandra images of N103B corresponding to the emission of oxygen (left, 0.5 – 0.7 keV), Fe-L (middle, 0.7 – 1.0 keV) and the Ar, Ca, Fe-K and continuum emission (right, 3 – 6.8 keV).

absoption corresponding to the O VIII (at 18.97 Å). Typical column densities of $10^{16}\mathrm{cm}^{-2}$ are found toward the high galactic latitude points. Within the accuracy these absorption feaures are not redshifted and their typical turbulent velocity is between 0 and 550 km $\mathrm{s}^{-1}$. When combined with recently measured emission line intensities of the same ions, we can obtain separate constraints on the density and length scale of the absorbing medium, which indicate that it is likely the intragroup medium of the Local group of Galaxies.

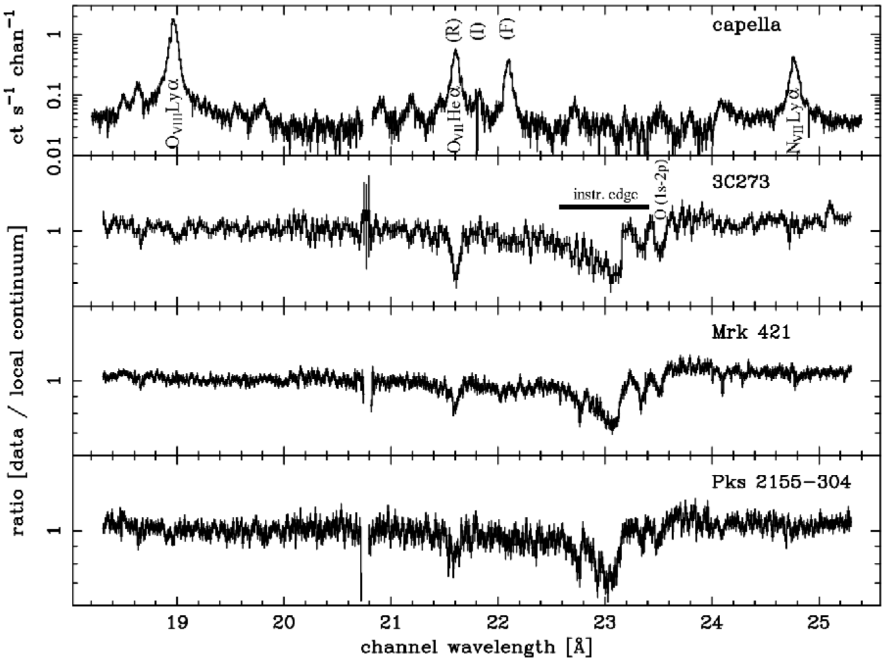


**Figure 21.** Absorption in the local IGM, note also the instrumental O-edge between 22.4 and 23.4 Å for which no correction is applied.

## ACKNOWLEDGMENTS

This work is based on observations obtained with *XMM-Newton*, an ESA science mission with instruments and contributions directly funded by ESA member States and the USA (NASA).

## REFERENCES

1. Branduardi-Raymont, G., Sako, M., Kahn, S.M. et al., A&A, 365, L140
2. Brinkman, A.C., Behar, E., Güdel, M., et al., A&A 365, L324, 2001
3. Brinkman, A.C., den Herder, J.W., Kahn, S.M. et al, ESA SP-488, 2002, in print
4. den Herder, J.W., Brinkman, A.C., Kahn, S.M., et al., A&A 365, L7, 2001
5. den Herder, J.W., Brinkman, A.C., Kahn, S.M. et al., ESA SP-488, 2002, in print
6. de Vries, C.P., den Boggende, A.J., den Herder, J.W. et al., in preparation for A&A
7. Güdel, M., Audard, M., Skinner, et al., in preparation, 2002, *and* in ESA SP-488, 2002, in print
8. Güdel, M., Audard, M., Smith, K.W., et al., 2002, ASP conf series (cool stars workshop 12)
9. Henke, B.L., Lee, P., Tanaka, T.J. et al.,1982, Atomic Data Nucl. Data Tables, 27, 1
10. Kaastra, J.S., Ferrigno, C., Tamura, T. et al., A&A 365, L99, 2001
11. Kahn, S.M., Leutenegger, M.A., Cottam, J. et al., A&A 365, 2001, L312-L317
12. Kinkwabhala, A., Sako, M., Behar, E. et al., ApJ 2002, accepted for publication
13. Peterson, J.R., Paerels, F.B.S., Kaastra, J.S. et al., A&A 365, L104, 2001
14. Porquet, D., Mewe, R., Dubau, J. et al, A&A 376, 1113, 2001
15. Rasmussen, A, Peterson, J.R., Audard, M., et al., these proceedings
16. Rasmussen, A, Kahn, S.M., Paerels, F.B.S., et al, in preparation
17. Sako, M. Kahn, S.M., Branduardi-Raymont, G. et al., 2002, ApJ submitted
18. Tamura, T., Kaastra, J.S., Peterson, J.R. et al., A&A 365, L87, 2001
19. van der Heyden, K., Behar, E., Vink, J., et al., A&A 2002, accepted for publication